

# Ocean Remote Sensing Using X-Band Shipborne Nautical Radar—Applications in Eastern Canada

**Weimin Huang\*, Eric W. Gill**

*Faculty of Engineering and Applied Science, Memorial University, NL, Canada*

*\*Corresponding author: E-mail: weimin@mun.ca*

## CHAPTER OUTLINE

|  |            |
|--|------------|
| <b>1. Introduction .....</b>                 | <b>248</b> |
| <b>2. Wave Algorithms .....</b>              | <b>249</b> |
| <b>3. Wind Algorithms.....</b>               | <b>250</b> |
| 3.1 Curve-Fitting-Based Wind Algorithm ..... | 251        |
| 3.2 Rain Effect Mitigation .....             | 253        |
| <b>4. Experimental Results .....</b>         | <b>253</b> |
| 4.1 Data Overview .....                      | 253        |
| 4.2 Wave Measurement Results.....            | 255        |
| 4.3 Wind Retrieval Results.....              | 257        |
| <b>5. Conclusion .....</b>                   | <b>261</b> |
| <b>Acknowledgments .....</b>                 | <b>262</b> |
| <b>References .....</b>                      | <b>262</b> |

## 1. INTRODUCTION

Ground-based high-frequency (3–30 MHz) surface wave radar (HFSWR) and X-band nautical radar (around 10 GHz) have been widely used in ocean remote sensing for three decades. HFSWR systems such as CODAR<sup>1</sup> and WERA<sup>2</sup> are able to monitor sea surface currents, winds, waves, and targets “over the horizon” due to the strong interaction between HF radio signals and ocean gravity waves (see recent applications in<sup>3–6</sup>). Unlike HFSWR, which is usually land-based to provide broad coverage at the expense of resolution, compact X-band radar covers the line-of-sight area with a spatial resolution as good as 5 m and can be deployed on ships. This enables X-band radar to be an ideal sensor to fill the nearby blind area (the first one or two ranges) of HFSWR or provide finer measurement for the area of interest.

Since Young et al.<sup>7</sup> first retrieved wave information and current velocity from X-band nautical radar images using a fast Fourier transform analysis, such radars have become widely accepted as cost-effective instruments with high spatial and temporal resolution for sea surface observation. The radar transmitted signals interact strongly with the ocean surface small-scale roughness through Bragg scattering.<sup>8</sup> These short waves are mainly generated by local wind regime.<sup>9</sup> Because the higher energy, long surface waves modulate the small-scale waves, which are predominantly responsible for the scattering at X-band, the backscattered signals contain features from which information regarding the wave spectrum,<sup>7,10–13</sup> and wind field<sup>14–17</sup> parameters and current velocity<sup>18–21</sup> may be determined.

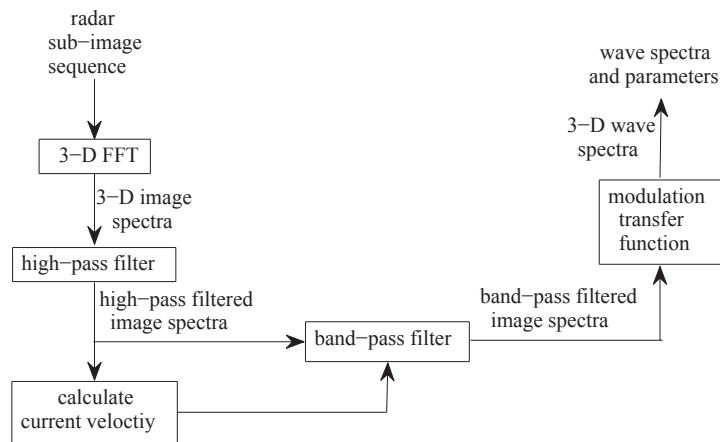
The commercial Wave Monitoring System (WaMoS),<sup>22</sup> developed expressly for extracting oceanographic parameters from X-band radar data, has been extensively deployed on ships and at fixed coastal sites. Successful experimental results have been widely reported. In Canada, the pioneering X-band nautical radar research work started in the early 1990s. The Grand Banks ERS-1 synthetic aperture radar (SAR) wave spectra validation experiment<sup>23</sup> evolved to compare the directional wave spectra obtained from five radar systems and two in situ buoys. Two of the five radars were X-band marine radars operated by the Royal Roads Military College and MacLaren Plansearch Incorporated, and wave analysis results were presented by Buckley et al.<sup>24</sup> Later, the Defence Research and Development Canada (DRDC) Atlantic conducted a number of sea trials off Halifax in 1993, 2004, 2006, and 2008<sup>25</sup> using MacRadar or WaMoS. In order to augment the limited open study on the data from these trials, wave and wind results retrieved from the data collected during the 2008 trial are presented here.

## 2. WAVE ALGORITHMS

X-band nautical radar backscatter is mainly due to Bragg scattering from centimeter-scale ocean waves<sup>8</sup> and wedge scattering from breaking waves on the long wave crests.<sup>9</sup> The backscatter signal is modulated by the long waves through tilt modulation and shadowing modulation.<sup>10</sup> Thus, the long wave information is mapped to the radar backscatter signals and may subsequently be extracted from the radar gray scale images.

Existing wave information extraction algorithms for nautical radar applications are based on 3-D FFT,<sup>7,10–12</sup> 2-D wavelet,<sup>13</sup> and shadow analysis<sup>26</sup> techniques. The flowchart of the traditional 3-D FFT method, which involves the following key steps, is shown in Figure 1:

1. Apply a 3-D FFT on a temporal sequence of radar subimages to generate 3-D image spectra.
2. Eliminate nonstationary and nonhomogeneous components by high-pass filtering the image spectra.
3. Execute an appropriate algorithm (e.g., Refs. 18–20) to obtain current velocity.
4. Extract the fundamental wave components with a band-pass filter (BPF) constructed based on the current-included dispersion relationship.

**FIGURE 1**

Flowchart of the traditional FFT-based wave algorithm.

5. Use a modulation transfer function to convert the filtered image spectra to wave spectra.
6. Derive wave spectra and their associated parameters.

It is clear this method always involves a BPF after the current velocity is obtained. An iterative least squares (LS)-based method that directly uses the classified fundamental and first-order harmonic wave components for wave spectra and parameter retrieval appears by Huang et al.<sup>27</sup> That method enables the elimination of the subsequent band-pass filter that is required to remove the non-wave contributions after the current velocity is obtained. Here, the simplified wave algorithm (without BPF), the details of which can be found by Huang et al.,<sup>27</sup> will be used and compared with the traditional method (with BPF).

### 3. WIND ALGORITHMS

The normalized radar cross-section (NRCS) has been shown to be dependent on wind speed<sup>9,28</sup> and direction.<sup>28,29</sup> For horizontally polarized (HH-polarized) radiation at grazing incidence, the NRCS was found to be maximum in the upwind direction and minimum in the crosswind direction,<sup>28,29</sup> changing nonlinearly with wind speed.<sup>14</sup> In 2003, Dankert et al.<sup>15</sup> proposed a method for extracting wind direction from quasi-stationary wind streaks and wind speed from the temporally integrated radar images along with the determined wind direction. This approach can be applied to shipborne radar data with geocoding that is required because extracting wind streaks is difficult due to the platform's horizontal motion.<sup>30</sup> A 180° directional ambiguity exists in the wind direction results. However, this ambiguity can be removed by extracting the movement of wind gusts visible in the radar image sequence.<sup>14</sup> Recently, two methods, which are independent of platform movement,

were developed by Lund et al.<sup>16</sup> and Vicen-Bueno et al.<sup>17</sup> The method proposed by Vicen-Bueno et al.<sup>17</sup> is referred to as a backscatter intensity-level-selection (ILS) algorithm, which determines wind direction and speed based on temporally integrated and spatially smoothed radar images and incorporates an empirical third-order polynomial geophysical model function (GMF). The least squares curve-fitting technique that was developed by Lund et al.<sup>16</sup> identifies the upwind peak based on the radar backscatter intensity dependence on the upwind direction and produces wind speed through an empirical third-order polynomial fit. In this chapter, the original curve-fitting-based algorithm and its modified version will be implemented.

### 3.1 CURVE-FITTING-BASED WIND ALGORITHM

For HH-polarized X-band radars operating at grazing incidence, the radar backscatter intensity varies with antenna look direction and has a single peak in the upwind direction.<sup>28,29</sup> In Lund et al.,<sup>16</sup> the dependence of radar backscatter gray scale intensity on antenna look direction is described by the cosine square function:

$$\sigma_{\theta} = a_0 + a_1 \cos^2(0.5(\theta - a_2)) \quad (1)$$

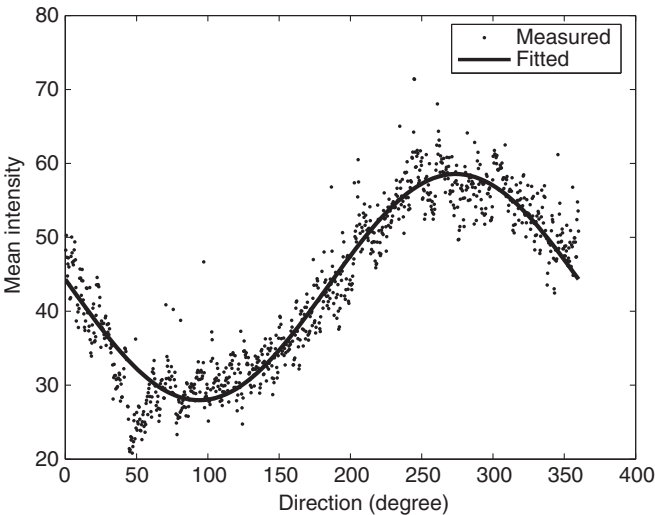
where  $a_i (i = 1, 2, 3)$  are the regression parameters, and  $\sigma_{\theta}$  represents the averaged radar gray scale intensity over a number of ranges (here from 450 to 1500 m) for an azimuthal direction  $\theta$ . The regression parameters  $a_i$  can be determined by curve fitting the measured range-averaged radar backscatter gray scale intensity and antenna look direction. Figure 2 depicts an example of the measured averaged backscatter intensity variation (dots) with antenna look direction and the best-fit curve (solid). After obtaining the curve-fitted model function of Eqn (1) for each individual radar image, the wind direction can be determined as the direction associated with the upwind backscatter peak. The upwind peak direction is actually given by the regression parameter  $a_2$  of the model in Eqn (1). This corresponds to the peak of the best-fit curve. It has been shown that this method works well even when some sections of the radar field of view are masked.<sup>16</sup>

The relationship between radar backscatter intensity and wind speed is assumed to follow an empirical third-order polynomial, which can be derived using the overall average radar backscatter intensity and the reference wind speed measured by other sensors (e.g., an anemometer).<sup>16</sup> Then, the radar wind speed results can be calculated from the measured overall average intensity value of Eqn (1). The overall average radar backscatter intensity  $\sigma_{avg}$  is defined as follows:<sup>16</sup>

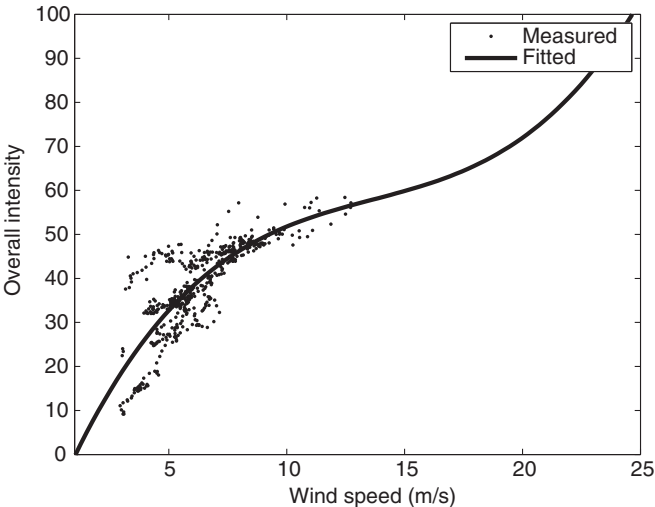
$$\sigma_{avg} = \frac{1}{2\pi} \int_0^{2\pi} a_0 + a_1 \cos^2(0.5(\theta - a_2)) d\theta. \quad (2)$$

Figure 3 shows the anemometer-measured wind speed results and the corresponding radar overall average backscatter intensities  $\sigma_{avg}$ . The best-fit curve (solid) indicated is derived using a least squares method based on a third-order polynomial function:

$$\sigma_{avg} = b_0 + b_1 U_{10} + b_2 U_{10}^2 + b_3 U_{10}^3, \quad (3)$$



**FIGURE 2**  
Range-averaged radar backscatter gray scale intensity as a function of antenna look direction.



**FIGURE 3**  
A scatter plot showing the relationship between the anemometer wind speed and the corresponding overall average radar backscatter intensity. The solid line represents the best-fit curve based on a third-order polynomial function using rain-free data.

as in Ref. 16 using rain-free data. Here  $b_i (i = 0, 1, 2, 3)$  represents coefficients to be determined by curve fitting, and  $U_{10}$  is the wind speed at 10 m above the sea surface.

### 3.2 RAIN EFFECT MITIGATION

It has been found that radar backscatter will be affected by rain through volume scattering and attenuation by raindrops in the intervening atmosphere as well as through changes in sea surface roughness resulting from rain impinging the ocean.<sup>31,32</sup> It is difficult to conclude whether the normalized radar cross-section is increased or decreased by rain because it depends on many factors such as rain rate, raindrop size, radar frequency, and polarization.<sup>31–33</sup> For X-band marine radar, it has been observed that sea surface radar backscatter is generally enhanced by the rain.<sup>16,34–36</sup> As a result, the radar-derived wind speed was found to be overestimated when using radar data collected in the presence of rain. In Ref. 16, Lund et al. presented a method to determine whether or not an image is contaminated by rain by analyzing the intensity histogram of the image. Rain-contaminated images were then discarded from their wind retrieval analysis. Here, a new technique for improving the extraction of wind speed from rain-contaminated data is proposed. The technique includes the following steps:

1. Because rain can strongly impact the number of pixels with zero intensity, the zero-pixel percentage (ZPP, i.e., the ratio, expressed as a percentage, of the number of image pixels with zero intensity to the overall number of pixels) is used to distinguish the rain-free and rain-contaminated images.
2. Two third-order polynomial functions for the relationship between overall average backscatter intensity and wind speed for rain-free and rain-contaminated cases based on least squares fitting with rain-free and rain-contaminated data, respectively, are obtained. Note that these two functions have the same format as Eqn (3), but with different coefficients.
3. Radar images are classified as rain-free and rain-contaminated according to their ZPPs. For the rain-free data, wind speed is retrieved using the rain-free wind speed model obtained in Step 2. For the rain-contaminated data, wind speed is determined using the rain-contaminated wind speed model.

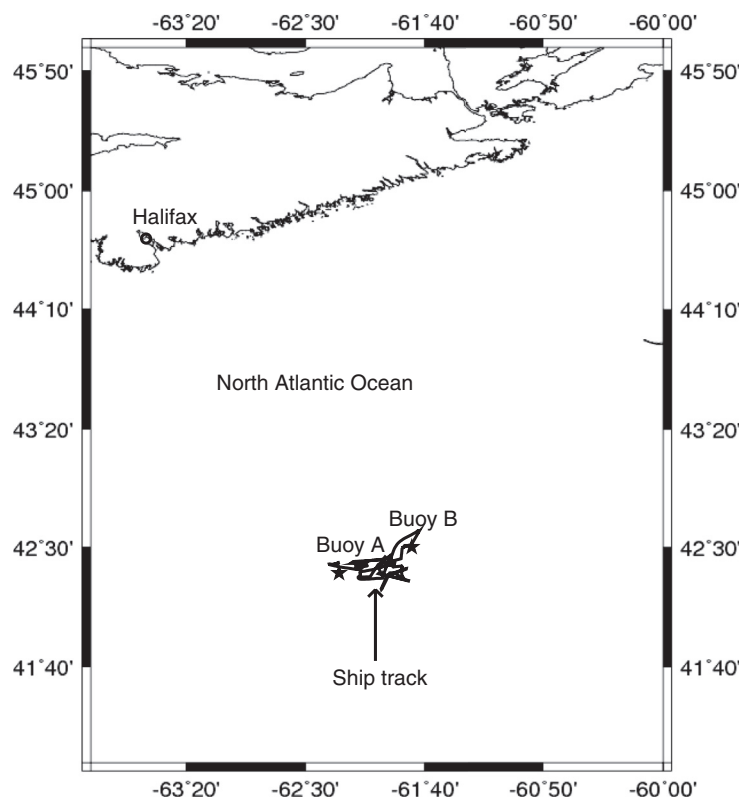
In what follows, this dual-wind-speed-model method is referred to as the two-model algorithm, and that involving the wind speed model derived from rain-free data alone is referred to as the single-model algorithm.

---

## 4. EXPERIMENTAL RESULTS

### 4.1 DATA OVERVIEW

In late November 2008, DRDC conducted a sea trial with the Canadian Navy research ship *CFAV Quest* in the Northwest Atlantic Ocean, approximately

**FIGURE 4**

Map of the experiment site. Stars represent wave buoys that are close to the GPS track of CFAV Quest.

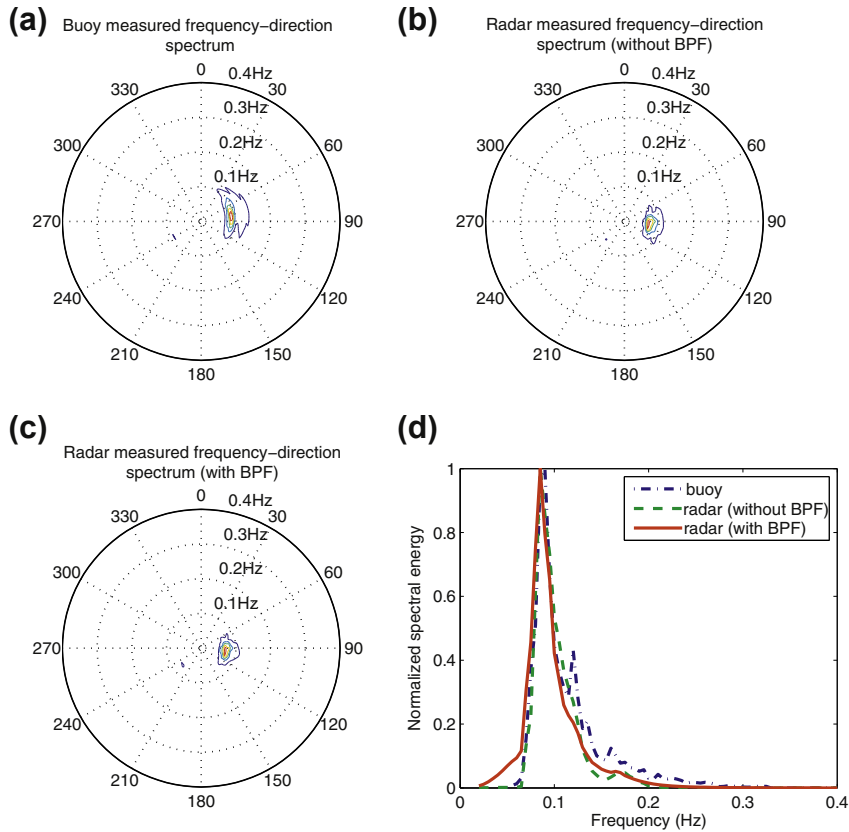
220 km from the coast of Halifax, Canada.<sup>25</sup> The water depth within the data collection area (near 42°30'N, 62°5'W, see Figure 4) is about 200 m and can be regarded as deep water. A standard ship-borne HH-polarized X-band (9.41 GHz) Decca BridgeMaster II 340 nautical radar and a nonacoustic data acquisition system (NADAS) recording data from two anemometers were deployed on the ship. The nautical radar, which was connected to a Wave Monitoring System II (WaMoS II),<sup>22</sup> covered 360° in azimuth with a beam width of about 2°. The useable range varied from 240 to 2160 m with a radial resolution of 7.5 m. The radar backscatter intensities were digitized and scaled into 8-bit unsigned integers ([0, 255]) by the WaMoS system. Every 32 radar images were sequentially combined into a single file. The time labels were in local standard time coordinates. The radar data collected during the period from 23:43 November 26 to 12:04 November 29 were used in the wave and wind algorithms here. During the sea trial, two nearby TRIAXYS wave buoys, deployed at 42°21'N, 62°15'W (buoy A) and 42°30'N, 61°45'W (buoy B), yielded wave data

averaged every half hour. Note that here only the wave data from the buoy that is closer to the ship are used for comparison with the radar wave results.

## 4.2 WAVE MEASUREMENT RESULTS

Both the traditional FFT-based wave algorithm and the simplified iterative LS-based method were applied to the radar data. Figure 5 shows the comparison of the radar-derived and buoy-recorded directional wave spectra  $E(f, \theta)$  and nondirectional wave frequency spectra  $E(f)$ . It can be seen that both the simplified algorithm and the traditional method agree well with the buoy measurements.

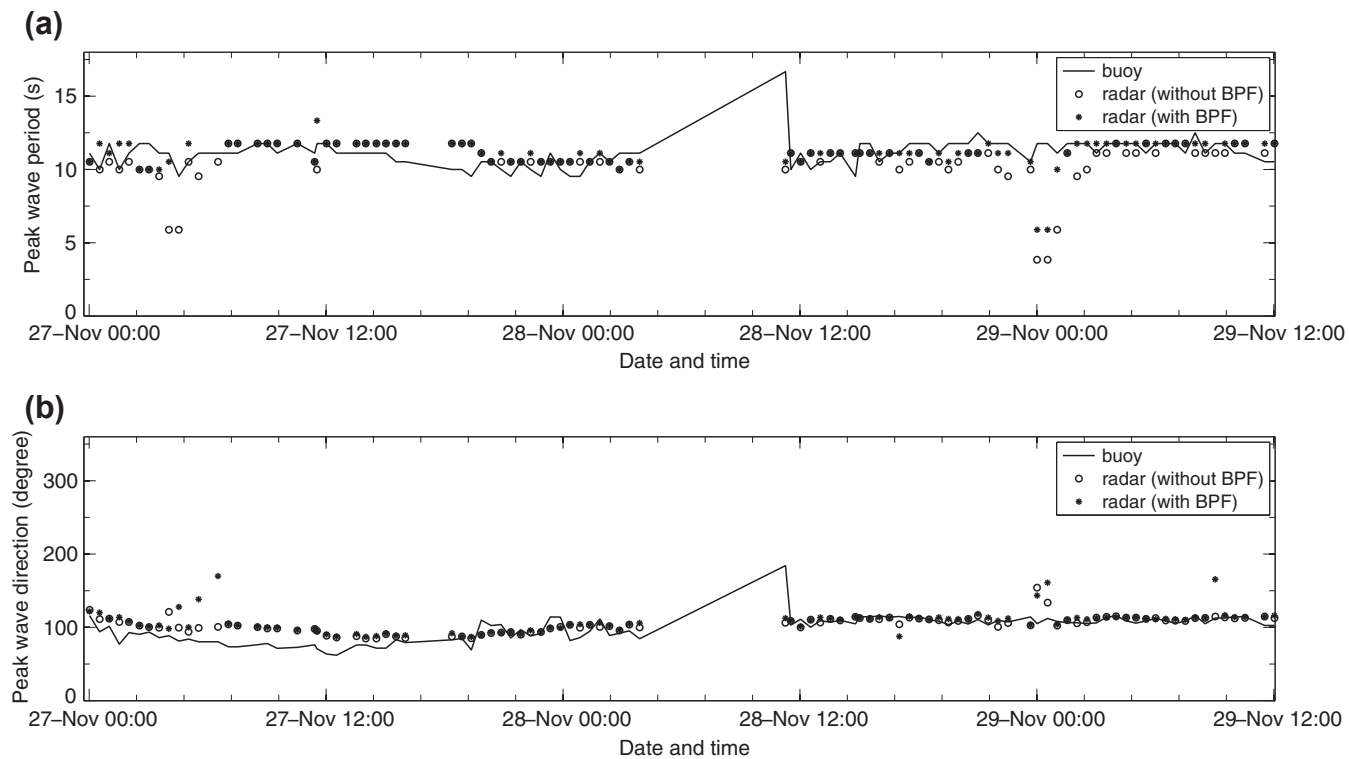
The peak wave direction and period results derived from the radar data using both the traditional and simplified algorithms are compared with the buoy-recorded result in Figure 6. Note that the radar results are averaged every half



**FIGURE 5**

Comparison of the radar-derived and buoy-recorded wave spectra: (a) buoy-recorded  $E(f, \theta)$ ; (b) radar-derived  $E(f, \theta)$  using the simplified algorithm (without BPF); (c) radar-derived  $E(f, \theta)$  using the traditional algorithm (with BPF); (d) 1-D wave frequency spectrum  $E(f)$ .



**FIGURE 6**

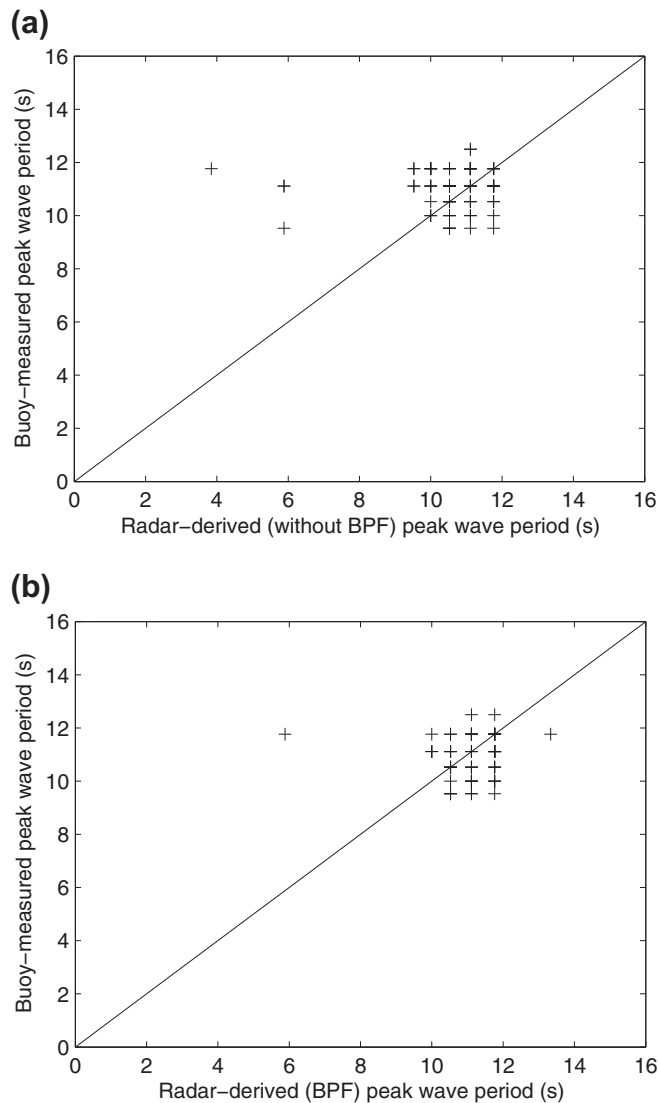
Comparison of radar-derived and buoy-recorded (a) peak wave period, and (b) peak wave direction.

hour for better comparison with the buoy data. From Figure 6, it can be seen that results from both algorithms agree well with the buoy result during most of the period. However, large deviation between the radar-derived and the buoy-recorded is observed for the time around 4:00 on November 27 and midnight of November 28. This is due to the low wind speed for these two periods (e.g., as shown in Figure 8(b), the wind speed is lower than 3 m/s from 23:40 on November 28 to 00:40 on November 29). It has been shown that a minimum sea surface wind speed of 3 m/s is required for HH-polarized operation to generate a usable level of backscatter for wave measurements.<sup>37</sup> As shown in Figure 8(c), the low-clutter direction percentages (LCDP, i.e., the number of low-clutter directions divided by the number of pulses as a percentage) of the images collected during that period are approximately 100%. Taking the buoy results as ground truth, the standard deviations (STDs) of the peak wave period obtained using the simplified and traditional wave algorithms are found to be 1.76 s and 2.19 s, respectively. Figure 6(b) illustrates that the peak wave direction results obtained using the simplified wave algorithm agree better with the buoy data than those from the traditional method. The corresponding STDs are  $14.7^\circ$  and  $18.6^\circ$ , respectively. The scatter plot in Figure 7 also shows the performances of these wave algorithms are comparable.

### 4.3 WIND RETRIEVAL RESULTS

Both the curve-fitting-based single-model and two-model wind algorithms described in Section 14.3 were implemented. The radar data considered here is classified as being contaminated by rain if the ZPP is below an empirical value of 10%. By utilizing this threshold, 9924 out of 49,182 images (i.e., 312 out of 1540 files) were identified as rain cases from the four-day dataset.

Figure 8 shows a typical comparison of the corresponding radar-derived and anemometer-measured wind results that were averaged over a 10-min interval. From Figure 8, it can be seen that both radar-deduced wind directions and speeds are affected by rain, and for the wind direction, the effect is relatively small. However, the radar-derived wind speed using the single-model algorithm was significantly overestimated as compared with the anemometer results. As mentioned earlier, the single-model method only involves the wind speed model (see Figure 3) obtained using the rain-free data. This means that the model is not applicable to rain-contaminated radar data. By using only the rain-contaminated data, the fitted wind speed model is depicted in Figure 9. From Figure 8, it is clear that the radar-derived wind speed results are improved significantly using the aforementioned rain mitigation scheme with two wind speed models. The error statistics are summarized in Table 1. By taking the anemometer wind data as ground truth, the rain mitigation scheme using two wind speed models (described in Step three) in Section 14.3.2 can reduce the wind speed STD and bias by 1.2 m/s and 1.3 m/s, respectively.

**FIGURE 7**

Scatter plot of (a) peak wave period: buoy-measured versus radar-derived (without BPF); (b) peak wave period: buoy-measured versus radar-derived (with BPF); (c) peak wave direction: buoy-measured versus radar-derived (without BPF); and (d) peak wave direction: buoy-measured versus radar-derived (with BPF).

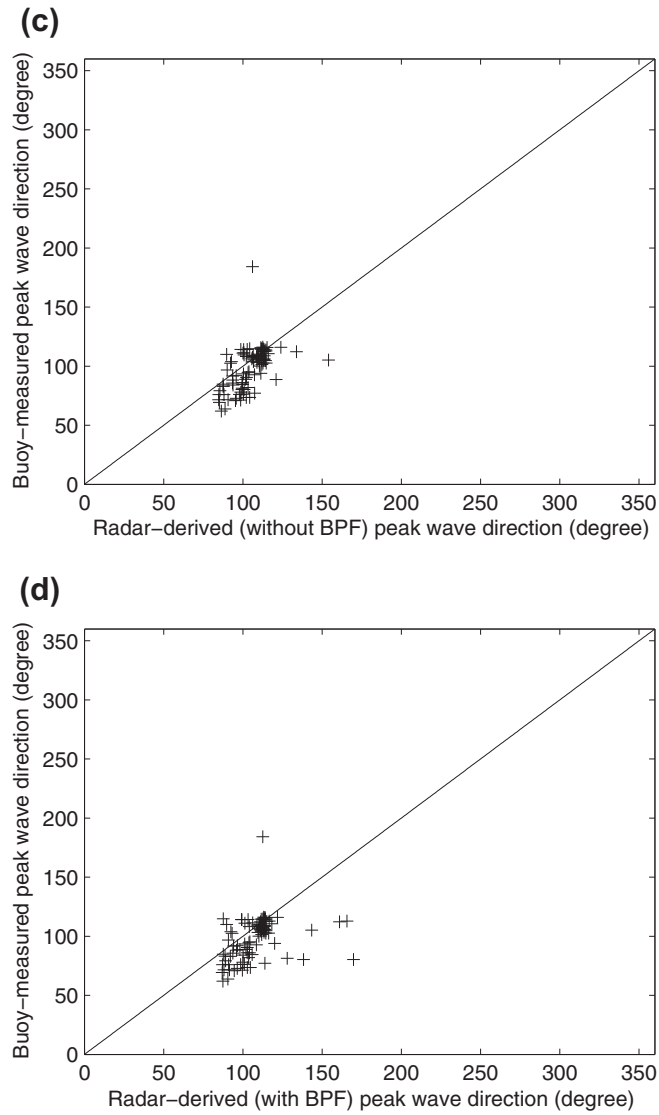
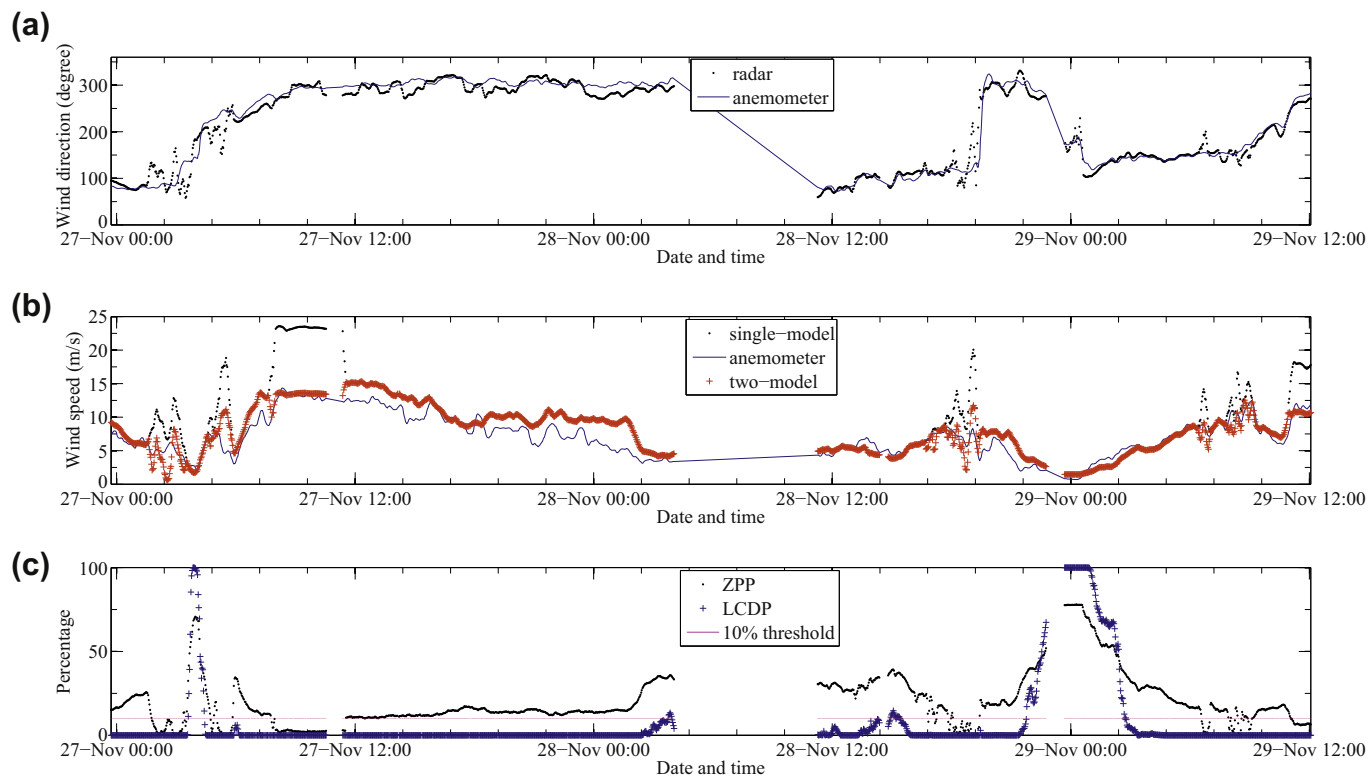
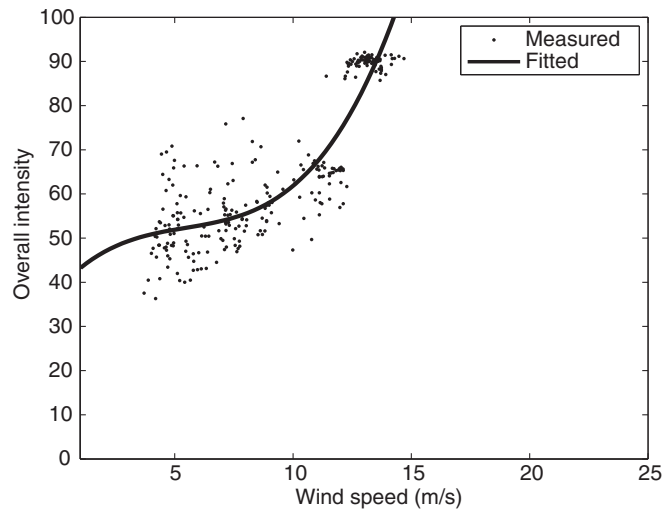


FIGURE 7 Continued

**FIGURE 8**

Results: (a) wind direction, (b) wind speed, and (c) zero pixel percentage (ZPP) and LCDP.

**FIGURE 9**

Scatter plot showing the anemometer wind speed, the corresponding radar backscatter intensity, and the best-fit curve based on a third-order polynomial function using rain-contaminated data.

**Table 1** Wind Speed and Direction Recovery Error Statistics: Bias and Standard Deviation (STD)

| Wind Algorithm | Wind Direction (degree) |      | Wind Speed (m/s) |     |
|----------------|-------------------------|------|------------------|-----|
|                | Bias                    | STD  | Bias             | STD |
| Single-model   | −3.8                    | 18.3 | 2.1              | 2.9 |
| Two-model      | −                       | −    | 0.8              | 1.7 |

## 5. CONCLUSION

Recent research work involving sea surface remote sensing using X-band nautical radar in Eastern Canada has been reviewed. Traditional and simplified FFT-based wave algorithms as well as the curve-fitting-based wind parameter extraction method have been investigated. In addition, a scheme incorporating two wind speed models (one for rain-free and one for rain-contaminated data) has been proposed to improve the wind speed retrieval results under rain conditions. These methods have been tested using shipborne nautical radar data collected during a recent sea trial in the Northwest Atlantic Ocean. On comparing the radar-deduced wave measurements with the buoy record, it is seen that the performance of the simplified iterative FFT-based algorithm is comparable to that of the traditional method. Also, a

comparison between the radar-measured wind results and the anemometer data confirms that the nautical radar can be a reliable tool for measuring sea surface wind parameters. The experimental results also show that the wind speed STD can be reduced by about 1.2 m/s using the rain-mitigation scheme with two speed models.

Although, here, the intention has been to develop an algorithm for improving wind speed from rain-contaminated radar data, it may also be seen from the foregoing analysis that the accuracy of wind direction measurement using X-band nautical radar decreases under rain conditions. In the future, a method for improving wind direction extraction from rain-contaminated radar data needs to be pursued. The work achieved here is expected to augment the existing utilities of X-band nautical radar for ocean remote sensing.

---

## ACKNOWLEDGMENTS

The authors thank Dr Eric Thornhill at Defence Research and Development Canada for providing the field data. This work was supported in part by the Research and Development Corporation (RDC) IRIF Ignite grant (207765) and a Natural Sciences and Engineering Research Council of Canada grant (NSERC 402313-2012) to Dr W. Huang, an NSERC grant (NSERC 238263-2010) to Dr Eric Gill and an Atlantic Innovation Fund (AIF) award to Memorial University (E. Gill: principal investigator), a Newfoundland and Labrador Innovation Business and Rural Development grant (IBRD 30-10921-008) to Dr Gill and Dr Huang.

---

## REFERENCES

1. Lipa BJ, Barrick DE. Least-squares methods for the extraction of surface currents from CODAR crossed-loop data — application at ARSLOE. *IEEE J Ocean Eng* 1983;**8**: 226–53.
2. Gurgel KW, Antonischki G, Essen HH, Schlick T. Wellen radar (WERA): a new ground-wave based HF radar for ocean remote sensing. *Costal Eng* 1999;**37**:219–34.
3. Liu Y, Weisberg RH, Merz CR. Assessment of CODAR SeaSonde and WERA HF radars in mapping surface currents on the west Florida Shelf. *J Atmos Ocean Technol* 2014;**31**: 1363–82.
4. Wyatt LR, Jaffres BD, Heron ML. Spatial averaging of HF radar data for wave measurement applications. *J Atmos Ocean Technol* 2013;**30**:2216–24.
5. Paduan JD, Washburn L. High-frequency radar observations of ocean surface currents. *Annu Rev Mar Sci* 2013;**5**:115–36.
6. Huang W, Gill EW, Wu X, Li L. Measurement of sea surface wind direction using bistatic high-frequency radar. *IEEE Trans Geosci Rem Sens* 2012;**50**:4117–22.
7. Young IR, Rosenthal W, Ziemer F. A three-dimensional analysis of marine radar images for the determination of ocean wave directionality and surface currents. *J Geophys Res* 1985;**90**(C1):1049–59.
8. Plant WJ, Keller WC. Evidence of Bragg scattering in microwave Doppler spectra of sea return. *J Geophys Res* 1990;**95**(C9):16,299–310.

9. Lee PHY, Barter JD, Beach KL, Hindman CL, Lake BM, Rungaldier H, et al. X-band microwave backscattering from ocean waves. *J Geophys Res* 1995;**100**(C2):2591–611.
10. Nieto-Borge JC, Rodriguez RG, Hessner K, Gonzales IP. Inversion of marine radar images for surface wave analysis. *J Atmos Ocean Technol* 2004;**21**:1291–300.
11. Izquierdo P, Guedes-Soares C, Nieto-Borge JC, Rodriguez GR. A comparison of sea-state parameters from nautical radar images and buoy data. *Ocean Eng* 2004;**31**:2209–25.
12. Nieto-Borge JC, Hessner K, Jarabo-Amores P, de la Mata-Moya D. Signal-to-noise ratio analysis to estimate ocean wave heights from X-band marine radar image time series. *IET Radar Sonar Navig* 2008;**2**:35–41.
13. An J, Huang W, Gill EW. A self-adaptive wavelet-based algorithm for wave measurement using nautical radar. *IEEE Trans Geosci Rem Sens* 2015;**53**:567–77.
14. Dankert H, Horstmann J, Rosenthal W. Wind- and wave-field measurements using marine X-band radar-image sequences. *IEEE J Ocean Eng* 2005;**30**:534–42.
15. Dankert H, Horstmann J, Rosenthal W. Ocean wind fields retrieved from radar-image sequences. *J Geophys Res Oceans* 2003;**108**(C11):16-1–16-11.
16. Lund B, Graber HC, Romeiser R. Wind retrieval from shipborne nautical X-band radar data. *IEEE Trans Geosci Rem Sens* 2012;**50**:3800–11.
17. Vicen-Bueno R, Horstmann J, Terril E, de Paolo T, Dannenberg J. Real-time ocean wind vector retrieval from marine radar image sequences acquired at grazing angle. *J Atmos Ocean Technol* 2013;**30**:127–39.
18. Gangeskar R. Ocean current estimated from X-band radar sea surface images. *IEEE Trans Geosci Remote Sens* 2002;**40**:783–92.
19. Serafino F, Lugni C, Soldovieri F. A novel strategy for the surface current determination from marine X-band radar data. *IEEE Geosci Remote Sens Lett* 2010;**7**:231–5.
20. Senet CM, Seemann J, Ziemer F. The near-surface current velocity determined from image sequences of the sea surface. *IEEE Trans Geosci Remote Sens* 2001;**39**:492–505.
21. Huang W, Gill EW. Surface current measurement under low sea state using dual polarized X-band nautical radar. *IEEE J Sel Top Appl Earth Obs Remote Sens* 2012;**5**:1868–73.
22. WaMoS II. *Wave and surface current monitoring system operating manual*. May 2012. version 4.0. [Online]. Available: [oceanwaves.org](http://oceanwaves.org).
23. Dobson FW, Smith SD, Anderson RJ, Vachon PW, Vandemark D, Buckley JR, et al. The Grand Banks ERS-1 SAR wave spectra validation experiment. In: *Proc. European Space Agency ERS-1 Symposium, Cannes, France*; 1992.
24. Buckley JR, Allingham M, Michaud R. On the determination of directional spectra from marine radar imagery of the sea surface. *Atmos Ocean* 1994;**32**:195–213.
25. Stredulinsky DC, Thornhill EM. Ship motion and wave radar data fusion for shipboard wave measurement. *J Ship Res* 2011;**55**:73–85.
26. Gangeskar R. An algorithm for estimation of wave height from shadowing in X-band radar sea surface images. *IEEE Trans Geosci Remote Sens* 2014;**52**:3373–81.
27. Huang W, Gill EW, An J. Iterative least-squares-based wave measurement using X-band nautical radar. *IET Radar Sonar Navig* 2014;**8**:853–63.
28. Hatten H, Ziemer F, Seemann J, Nieto-Borge J. Correlation between the spectral background noise of a nautical radar and the wind vector. In: *Proc. 17th Int. Conf. Offshore Mechanics and Arctic Eng. (OMAE), Lisbon, Portugal*; 1998.
29. Trizna D, Carlson D. Studies of dual polarized low grazing angle radar sea scatter in nearshore regions. *IEEE Trans Geosci Remote Sens* 1996;**34**:747–57.



30. Lund B, Graber HC, Horstmann J, Terrill E. Ocean surface wind retrieval from stationary and moving platform marine radar data. In: *Proc. IEEE IGARSS, Munich, Germany*; 2012. p. 2790–3.
31. Tournadre J, Quilfen Y. Impact of rain cell on scatterometer data: 1. Theory and modeling. *J Geophys Res* 2003;**108**(C7):18-1–18-14.
32. Contreras RF, Plant WJ. Surface effect of rain on microwave backscatter from the ocean: measurements and modeling. *J Geophys Res* 2006;**111**(C08):C08019.
33. Melsheimer C, Alpers W, Gade M. Investigation of multifrequency/multipolarization radar signatures of rain cells over the ocean using SIR-C/X-SAR data. *J Geophys Res* 1998;**103**(C9):18867–84.
34. Braun N, Gade M, Lange PA. Radar backscattering measurements of artificial rain impinging on a water surface at different wind speeds. In: *Proc. IEEE IGARSS, Hamburg, Germany*; 1999. p. 200–2.
35. Liu Y, Huang W, Gill EW. Analysis of the effects of rain on surface wind retrieval from X-band marine radar images. In: *Proc. MTS/IEEE oceans*. Canada: St John's; 2014.
36. Liu Y, Huang W, Gill EW, Peters DK, Vicen-Bueno R. Comparison of algorithms for wind parameters extraction from X-band shipborne marine radar images. *IEEE J Sel Top Appl Earth Obs Remote Sens* 2015;**8**:896–906.
37. Nieto-Borge JC, Guedes-Soares C. Analysis of directional wave fields using X-band navigation radar. *Coast Eng* 2000;**40**:375–91.